Mesoscale Chemomechanical Interplay of the $LiNi_{0.8}Co_{0.15}Al_{0.05}O_2$ Cathode in Solid-State Polymer Batteries

Münir M. Besli,[†,‡] Sihao Xia,[§] Saravanan Kuppan,[*,†] Yiqing Huang,[∥] Michael Metzger,[†] Alpesh Khushalchand Shukla,[⊥] Gerhard Schneider,[‡,#] Sondra Hellstrom,[†] Jake Christensen,[†] Marca M. Doeff,[*,%] and Yijin Liu[*,§]

[†]Robert Bosch LLC, Research and Technology Center, Sunnyvale, California 94085, United States

[‡]Department of Mechanical Engineering, Karlsruhe Institute of Technology (KIT), Karlsruhe 76131, Germany

[§]Stanford Synchrotron Radiation Lightsource, SLAC National Accelerator Laboratory, Menlo Park, California 94025, United States

[∥]Seeo Inc., Hayward, California 94545, United States

[⊥]National Center of Electron Microscopy, Molecular Foundry, Lawrence Berkeley National Laboratory, Berkeley, California 94720, United States

[#]Materials Research Institute, Aalen University, Aalen 73430, Germany

[%]Lawrence Berkeley National Laboratory, Energy Technologies Area, University of California, Berkeley, Berkeley, California 94720, United States

ABSTRACT: Complex chemomechanical interplay exists over a wide range of length scales within the hierarchically structured lithium-ion battery. At the mesoscale, the interdependent structural complexity and chemical heterogeneity collectively govern the local chemistry and, as a result, critically influence the cell level performance. Here we investigate the morphology and state of charge (SOC) inhomogeneity within secondary NCA particles that were cycled in solid polymer batteries. We observe substantial inhomogeneity in the nickel oxidation state (a proxy for SOC) and loss of structural integrity within secondary particles after only 20 cycles due to significant intergranular cracking. The formation of mesoscale cracks causes loss of ionic and electrical contact within cathode particles, triggering increases in local impedance and rearrangement of transport pathways for charge carriers. This can eventually lead to deactivation of subparticle level domains in solid-state lithium-ion batteries. Our findings highlight the importance of proper mesoscale strain and defect management in polymer lithium-ion batteries.

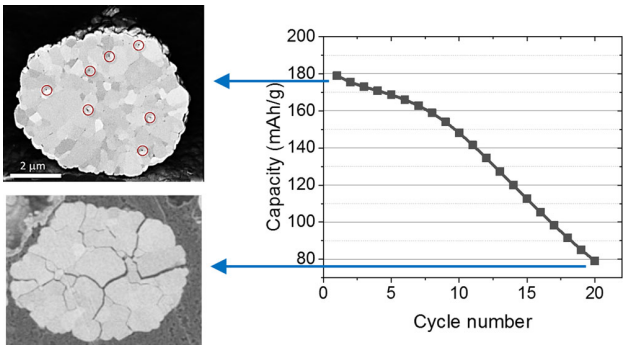

INTRODUCTION

Since the introduction of the lithium-ion battery (LiB) almost three decades ago, this energy storage device has been broadly adapted in many applications spanning from consumer electronics to electric vehicles (EVs)[1−3] thanks to its advantages in energy density, power density, and cycle life compared to other commercially available battery technologies.

While energy density and cycle life are critical factors, safety is another vital aspect that needs to be seriously considered in battery development, particularly for application in EVs. The cost of getting a battery wrong can be colossal. Currently deployed state-of-the-art LiBs generally contain a nonaqueous, liquid electrolytic solution that is composed of organic, flammable components. It is highly desirable to replace the currently used liquid electrolytes with a solid-state electrolyte (SSE), such as a polymer or a ceramic,[4,5] because of the inherent safety advantages, including the decreased flammability,[6] the absence of leakage, and the high resistance to mechanical shocks and vibrations.[7] Automakers around the world consider solid-state batteries to be the next generation of devices that can potentially improve the safety, range, and affordability of electric vehicles. SSEs could also make it feasible to use lithium metal as an anode instead of graphite, thanks to their enhanced dendrite penetration resistance. As a result, the use of SSEs could facilitate the battery chemistries that were not practical in conventional LiBs due to safety problems caused by dendritic deposition of lithium metal during the charging process.[8] The combination of a lithium metal anode, a solid electrolyte, and the commercially predominant class of cathode active materials (CAMs), e.g.,

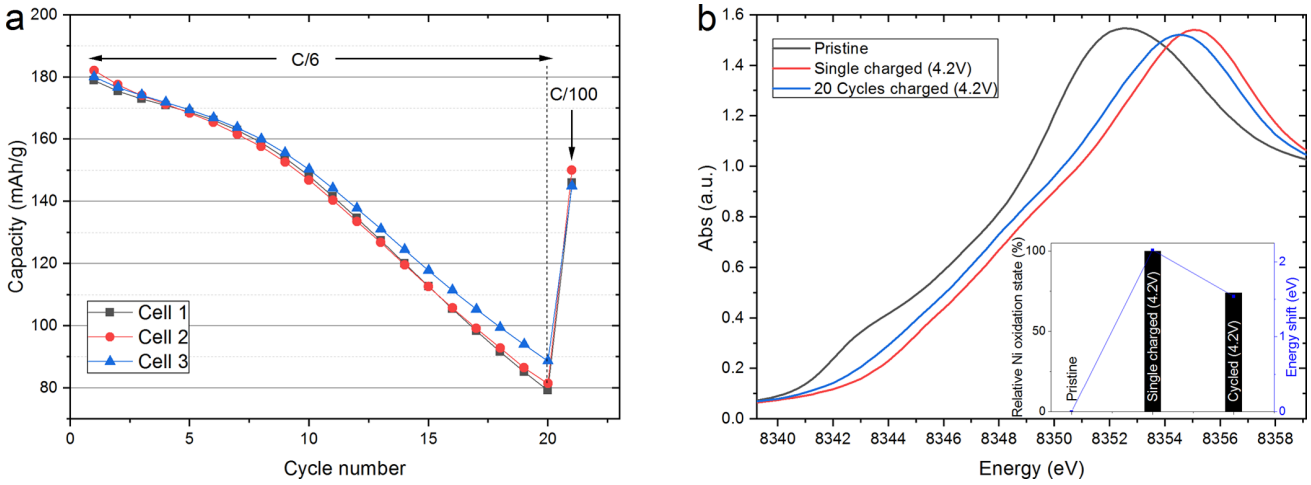

Figure 1. (a) Specific capacities for three cells as a function of the cycle number. Cells cycled with a C/6 rate (cycles 1−20) show significant capacity loss at 80 °C (180.36 mAh/g → 83.09 mAh/g). Cycling with decreased current density (C/100, cycle 21) results in partial recovery of the initially lost capacity (83.09 mAh/g → 146.98 mAh/g); however, a significant part of the capacity is irreversibly lost. (b) Ni K-edge XANES spectra for pristine, charged, and cycled electrodes. The nickel absorption edge for cycled electrodes is shifted to the left that the cycled electrode is reduced compared to the electrode charged only one time.

the layered nickel-rich oxides (LNOs), could be a viable pathway toward next generation solid-state LiBs with compelling advantages in energy density and safety.

Although LNOs such as $LiNi_{0.8}Co_{0.15}Al_{0.05}O_2$ (NCA) and $LiNi_xCo_yMn_zO_2$(NCM) offer high reversible capacity and good rate capabilities,[9] their inherent structural and thermal instability can impact cycle life under some conditions.[9] LNOs, which are commonly prepared by a simple and cost-effective coprecipitation method, are often in the form of spherical secondary particles that consist of many submicrometer-sized and densely packed primary particles (grains). This mesoscale architecture is susceptible to a degradation mechanism involving crack formation and decrepitation.[10−15] In conventional LIBs, through the process of repeated intercalation and deintercalation of lithium ions, intergranular fractures (i.e., microcracks[12]) develop along the grain boundaries of the primary particles upon electrochemical cycling. This phenomenon is often attributed to anisotropic crystal volume change.[16−20] Several models of lithium intercalation suggest that fracturing can be driven by diffusion-induced stress, which increases with (de)intercalation current density and particle size, as well as abrupt two-phase lattice constant changes.[21−24] Even though the intergranular cracking can already be observed after only a few cycles,[11,16] the degree generally changes as a function of the cycle number,[18,25] the upper cutoff voltage,[26−28] operating temperature,[15] C-rate[29] and storage time.[30] Intergranular fracturing can result in reduced electrical contact of active material and, thus, increased electrical resistance[18] and intensified side reactions, e.g., electrolyte decomposition and transition metal dissolution,[11,16,31] due to the increase in the exposed electrode surface area. These effects collectively expedite capacity fade and impedance rise in the cell.

Although many studies have investigated particle-cracking-induced cathode degradation in LiBs with liquid electrolytes, not much is known about these phenomena in solid-state battery configurations. As liquid electrolyte can infiltrate cracks, diffusion may be preserved due to the migration of lithium ions through newly developed active interfaces.[29] For similar reasons, Li and active material loss due to formation of these new interfaces may play a larger role. By comparison, loss of ionic connectivity is expected to dominate the system in solid-state batteries. Poor contact between solid electrolyte and the outer surface of the secondary active material particle may result in higher current density inhomogeneity, thereby hastening the onset of stress-induced particle fracture compared to conventional liquid electrolyte-based cells. Poor effective diffusion of lithium in the fractured particles without liquid electrolyte could further accelerate degradation as the better connected portions of the particle experience ever increasing local current density.

Herein, we identify and evaluate intergranular cracking in composite NCA/poly(ethylene oxide) (PEO) cathodes. By means of two- and three-dimensional nanoscale full-field (FF) transmission X-ray microscopy (TXM) and focused ion beam/broad ion beam scanning electron microscopy (FIB/BIB-SEM), we investigate the morphological defects and chemical heterogeneity in secondary NCA particles. We map out the spatial distribution of the nickel oxidation state using X-ray absorption near-edge spectroscopy imaging (XANES), which serves as an indicator to quantify the local state of charge (SOC). Our experimental results indicate that severe intergranular cracking in NCA particles cast in PEO develops after only 20 cycles. We also estimate the diffusion deterrent via a numerical model that calculates the disruption in the diffusion lithium pathways caused by cracking and the corresponding impact on primary grain accessibility within the secondary particles. Our findings highlight the importance of proper mesoscale strain and defect management in polymer lithium batteries.

RESULTS AND DISCUSSION

Electrochemistry. Figure 1a shows the capacity fade for three NCA-PEO//lithium cells upon cycling at a rate of C/6 at 80 °C. After only 20 cycles, a significant drop in capacity (180.36 mAh/g to 83.09 mAh/g) is observed. This represents a 46.07% retention of initial capacity. By comparison, a liquid NCA cell cycled 140 times at the same rate has a capacity retention of 89.89% (Figure S1). Upon further investigation,

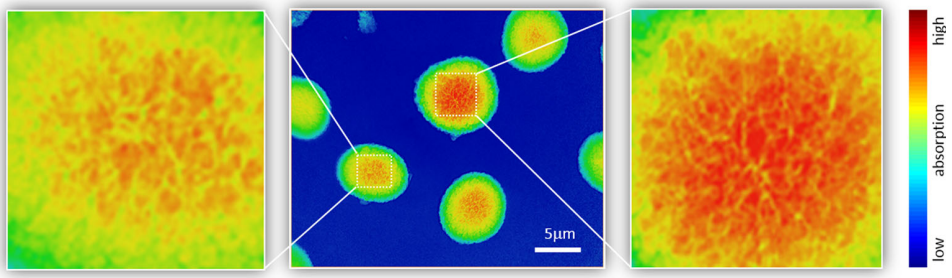

Figure 2. Color-coded 2D-FF-TXM transmission images with enlarged areas for two secondary particles harvested from cells cycled 21 times. Because of the sphericity of the particles, the overall intensity profiles over the particles show a higher absorption at the core. The irregular patterns, on the other hand, highlight the fine intergranular cracks developed upon electrochemical cycling.

72.19% of the lost capacity in the NCA-PEO cells can be recovered by cycling at a rate of C/100 (see Figure S2 for charge/discharge curves). The slow rate cycling minimizes kinetic effects and therefore allows greater access to available capacity in regions of high impedance. To support the slow rate cycling measurements, electrochemical impedance spectroscopy (EIS) as shown in Figure S3 additionally reveals an increase in the first semicircle after only 20 cycles, again suggesting an increase in the impedance of ion diffusion and electron transfer.

Evidently, there exist degradation mechanisms in the NCA-PEO cells that lead to capacity loss much more quickly than in their liquid cell counterparts, and the greater part of these mechanisms in the short term are associated with impedance growth rather than simple decomposition of active material. Thermal degradation of the CAM at elevated temperature,[32,33] the well-established electrochemical oxidation of the PEO electrolyte above ∼4 V,[34] delamination of interfaces due to gas generation, and corrosion of the Al current collector,[35] as well as mechanical failure of the CAM via fracture, are all plausible mechanisms that may contribute to impedance growth and capacity loss. However, it may also be expected that different mechanisms will result in different distributions of affected active material throughout a cathode secondary particle and throughout a cell, so observation of the 3D distribution of redox-active Ni in affected CAM material should provide some useful disambiguation.

Bulk XANES analysis. Ni redox is the main charge compensation for Li insertion/extraction in LNOs and can be used as a proxy for state-of-charge in the electrode.[36] We conducted X-ray absorption near-edge spectroscopy (XANES) experiments to investigate the nickel oxidation state in the bulk cathode material to help disambiguate the origin of the drastic capacity loss. Figure 1b shows the nickel K-edge XANES spectra of pristine cells and those charged once to 4.2 V or cycled repeatedly (21 cycles; 20 cycles at *C*/6, last cycle at *C*/100) and stopped fully charged (4.2 V). Spectra of the polymer cells were collected at beamline 4-1 of the Stanford Synchrotron Radiation Lightsource (SSRL) ex situ, i.e., after cycling concluded. Spectra collected from the pristine cell and the cell charged once were used as reference spectra for the cells in the reduced and oxidized states, respectively. While the Ni valence state in the pristine cell is 3+, it is 3.7+ in the charged cell, using the reasonable assumption that Ni redox accounts for the majority of the charge compensation.[36]

The spectrum of the cycled electrode appears to be intermediate between that of the pristine and the charged cells. A shift to lower energy suggests a decrease in the average bulk nickel oxidation state in the charged electrode that was cycled 21 times. To quantify the reduction that takes place in the cycled NCA-PEO cell, we used the edge position, defined by photoelectron energy origin (E_0), a commonly used parameter for extracting edge energy level in XANES spectra.[37] Our results suggest that the relative oxidation state of the bulk material in cycled electrodes is ∼71.4% of the initial oxidation state of the charged electrode, indicating a reduction by nearly 30% (see Figure 1b, inset). The reduction of the bulk Ni oxidation state suggests diminished charging of the cathode, which could be caused by oxygen evolution, phase transformation, and/or disconnection and isolation of active material in the composite.

While the bulk XANES informs us of an overall decrease in Ni oxidation state, the two- and three-dimensional distribution of redox activity in these NCA particles will provide more specific information as to probable origins of this capacity loss. For example, in conventional LiBs, the electrode−electrolyte interaction on the surface of secondary particles and the associated electrolyte decomposition lead to a significant reduction of nickel redox activity at the particle surface.[17] Using depth-sensitive characterization techniques, several groups have shown that the surface of LNO particles is more prone to the degradation reactions than the bulk.[38−41] Surface degradation on the CAM also makes sense if capacity loss is a result of irreversible oxidation of the polymer electrolyte at the interface with the cathode at high potentials.[34,42] On the other hand, CAM fracture, especially in a solid-state battery (SSB) system where electrolyte cannot flow, ought to result in the opposite distribution—surface grains still connected to electrolyte will remain redox active, while disconnected grains deep in the particle bulk will not. Finally, delamination or corrosion of a current collector, while increasing the impedance of the cell overall, should not alter the redox activity profile within a CAM particle. By performing 2D and 3D full-field transmission X-ray microscopy with XANES, we aim to further understand both the electrochemical capacity loss and the diminished bulk oxidation state observed in NCA-PEO cells after only a few cycles.

2D-FF-TXM-XANES. To identify any mechanical changes in the CAM, i.e., the formation of intergranular cracks within the secondary NCA particles, as a first step, we employed two-dimensional full-field transmission X-ray microscopy (2D-FF-TXM).[43] With a nominal spatial resolution of ∼30 nm, this technique is capable of visualizing the evolution of cracks within secondary particles. For statistical accuracy, we imaged a

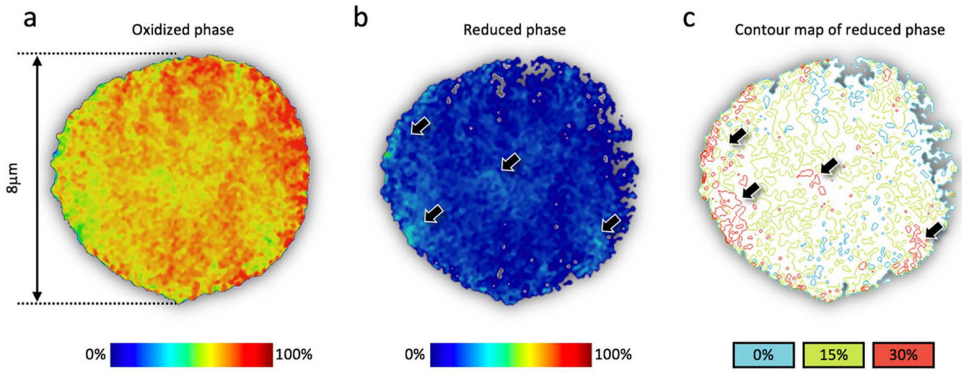

Figure 3. 2D-FF-TXM chemical mapping of a cycled (21 cycles) and fully charged NCA particle. The spatial distributions of the oxidized phase (a) and the reduced phase (b) highlight isolated regions within the secondary particle. The contour map of the reduced phase (c) shows the isolated regions in more detail.

large number of secondary particles (see Figure 2 for a representative image and Figure S4 for more particles), which were harvested from fully charged (4.2 V) polymer NCA cells after 21 cycles. The contrast in the 2D-FF-TXM projection images is directly proportional to the mass thickness of the particles and is color-coded to the color map in Figure 2. The 2D projection images represent the accumulated absorption through the depth of the spherical particles. The overall intensity profile of all the particles exhibits higher absorption near the center region due to the relatively larger thickness along the beam direction. An irregular pattern caused by the morphological changes can be clearly observed throughout the particles. Severe cracking is particularly evident in the center regions, as highlighted in the two magnified views in Figure 2. Although the projection images do not offer any depth resolution, the lateral spatial resolution of around 30 nm can still facilitate the observation of electrochemical cycling induced cracks in the secondary particles, irrespective of the particle form, diameter, and sphericity.

The observed morphological degradation can hinder ion diffusion leading to impedance growth and irreversible capacity loss. To understand how the fracturing influences the lithium ion migration within the secondary particles, 2D and 3D spatial distributions of the nickel oxidation states in the cycled cells were mapped in a series of FF-TXM-XANES studies using beamline 6-2c at SSRL. Details about the experimental setup, the elemental sensitive imaging, FF-TXM-XANES and the data processing software, known as TXM-Wizard, can be found in the literature.[44−46] Figure 3 shows a summary of our 2D-FF-TXM-XANES studies, which offer a direct visualization of the 2D mapping of the XANES data over the Ni K-edge. The spatial distributions of the oxidized and the reduced chemical species are calculated by means of linear combination fitting of the spatially resolved XANES data to the spectroscopic fingerprints of the two known principal chemical components, i.e., the Ni K-edge XANES spectra of particles from the single charged and the pristine cells. Both maps are color coded to the relative concentration of the respective species; e.g., for the oxidized phase, a 100% fit with the oxidized fingerprint derived from the charged cell is indicated by a dark red color and no fit by a dark blue color; for the reduced phase map, a 100% fit with the spectroscopic fingerprint used for fitting (pristine NCA) is indicated by a red color; no fit, by a dark blue color.

Although the cycled cell was disassembled in the fully charged state, the maps shown in Figure 3a,b illustrate that in both the surface and the core regions within this particle (see black arrows in Figure 3b) several domains remain partially discharged. For a better visualization, we show in Figure 3c the contour map of the reduced phase over the investigated particle. The contour lines in Figure 3c are color coded to the relative concentration of the reduced phase, i.e., blue represents a relative concentration of 0%, green 15%, and red 30%. While the entire particle seems partly reduced, the isolated red (more reduced) islands in Figure 3c suggest that the partially deactivated domains are developed in a rather heterogeneous manner upon electrochemical cycling.

3D-FF-TXM. The observation of the cycling-induced particle fracturing and SOC heterogeneity by the 2D-FF-TXM method has important implications as discussed above. The correlation between the morphological degradation and the incomplete subparticle domain charging is, however, not obvious in the depth averaged imaging data (2D) due to the lack of spatial resolution along the beam direction. For better understanding of the chemomechanical interplay at the mesoscale (within the secondary NCA particle), we performed a 3D-FF-TXM-XANES study[45,47] to reveal the 3D evolution of the cracks and their successive impact on the heterogeneous distribution of the Ni oxidation state and, thus, that of the SOC within the particle.

The results on a cycled and fully charged secondary NCA particle are shown in Figure 4. Figure 4a presents the 3D rendering of the X-ray nanotomographic data of the particle. A few virtual slices through different depth of the particle are highlighted in the middle of Figure 4a to reveal more morphological details throughout the particle. Unlike for the 2D projection imaging data shown in Figures 2 and 3, each virtual slice derived from the 3D-FF-TXM measurement is of single-pixel (~30 nm) thickness. It is clear that isolated voids (highlighted by the red circles) are scattered throughout the entire particle. Additionally, the interconnected crack network (blue arrows) is more distinct near the particle's core. Direct visualization of Figure 4a indicates that the cracks likely originate in the core region[48] of the particle and propagate toward the particle surface. We point out here that in addition to the relative large crack network (blue arrows) fine and less visible crack patterns can also be observed throughout the particle (Figure 4a). These fine cracks are less visible because they are likely near or beyond the spatial resolution limit of the 3D-FF-TXM. Our 3D morphological study is in accordance with a recent high-resolution transmission electron microscopy

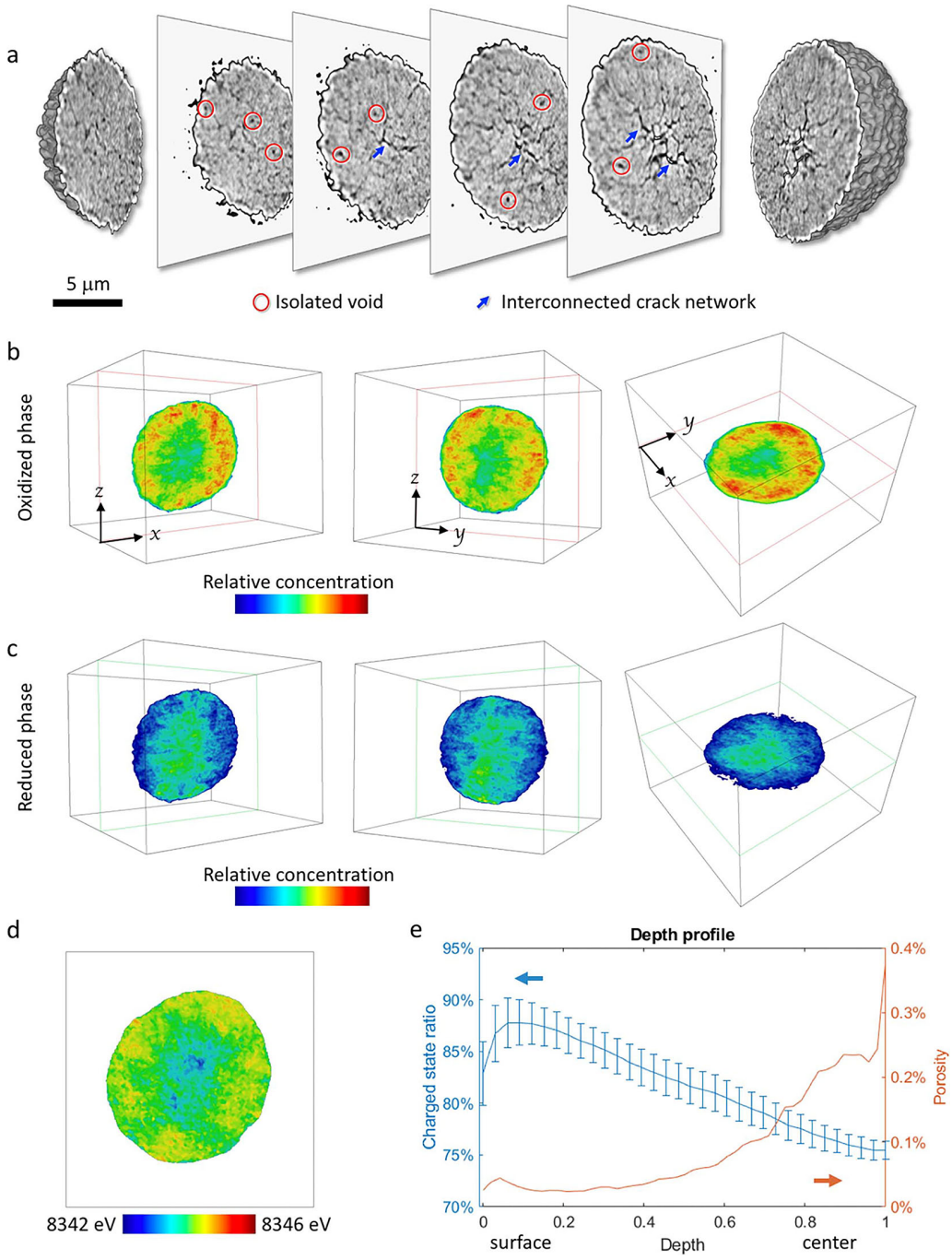

Figure 4. 3D chemical mapping of a cycled (21 cycles) and fully charged NCA particle. (a) 3D rendering of the nanotomographic data of the particle collected at 8 keV with four virtual slices showing the complexity of morphological defects. Isolated voids are marked with red circles, and the interconnected crack network is marked with blue arrows. (b, c) Chemical phase maps of the oxidized and the reduced phase, respectively, over the virtual slices in different orientations. (d) Edge energy map over the *XZ* plane denoted in (b). (e) Depth profile of the SOC and the porosity over the investigated particle using the *XZ* plane denoted in (b).

(HRTEM) study,[49] in which the authors demonstrate how the formation of a rock-salt phase in the core of NCA particles serve as a source for the observed degradation through intragranular cracking.

Although the spatial resolution of the 3D-FF-TXM-XANES is limited to tens of nanometers, it is capable of correlative structural and chemical imaging, which can offer a direct evidence for the mesoscale interplay of the morphological and chemical evolutions. The electrochemical effect of cracking within the NCA particle is visualized in Figure 4b,c. As with the 2D chemical mapping shown in Figure 3, chemical maps for the oxidized and reduced phase were obtained for the entire NCA particle by fitting the extracted XANES spectra of every single voxel ($32.5 \times 32.5 \times 32.5$ nm^3) to the spectroscopic fingerprints of the pristine NCA and the NCA charged once. Virtual slices of the color-coded 3D renderings for the oxidized and reduced phase are illustrated in three orthogonal planes labeled *XZ*, *YZ*, and *XY*. The virtual slices in

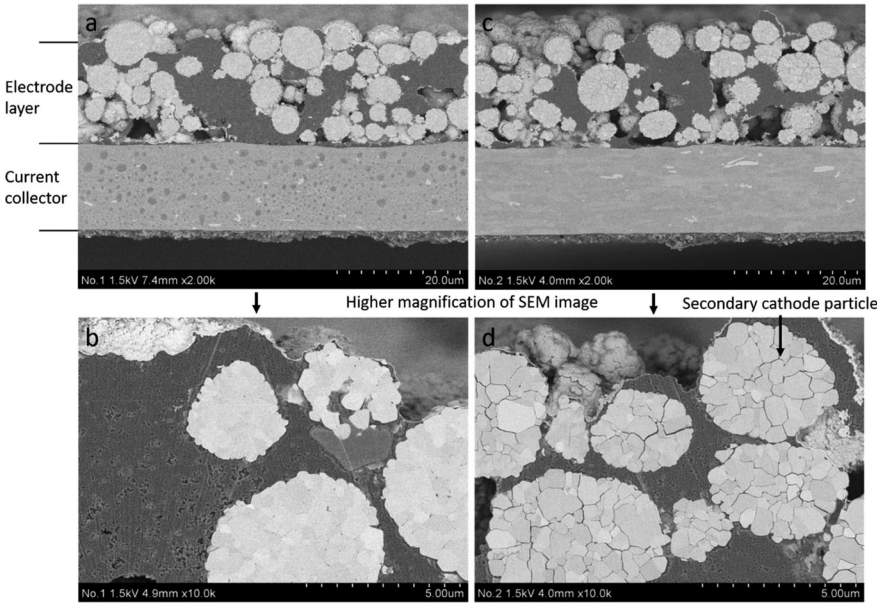

Figure 5. BIB-SEM observation of pristine and cycled (21 cycles, charged state) polymer electrode cross sections. (a) SEM cross-sectional images for pristine NCA electrode with higher magnification shown in (b). (c) SEM cross-sectional image for cycled NCA electrode with higher magnification shown in (d).

Figure 4b,c depict that while the particle shell is still electrochemically active, a significantly large, electrochemically less active core has formed after cycling. This observation provides a correlation between the cracks within the particle and the loss of electrochemical activity. The probability of isolation of primary grains within the core of the secondary particle by intergranular cracking is higher than for domains in the outer rim of the secondary particle. This results in partially deactivated inner grains that can no longer fully participate in the intercalation process, even when being charged with a very slow *C*-rate such as *C*/100 (see Figure 1a).

It is important to note that Figure 4b also reveals considerably reduced redox activity in the outermost layer of the secondary particle as well as in the core. The *XZ*, *YZ*, and *XY* planes that are shown resemble onions; the surface (a shell) and the core remain similarly reduced, while a layer of redox-active CAM sits in between. We hypothesize that the diminished redox activity in the shell and the core come from two different degradation phenomena. Reduction of the outermost layer, as previously discussed, is consistent with electrode–electrolyte interaction on the surface of secondary particles and the associated electrolyte (and CAM) decomposition as is also observed in conventional LiBs. By contrast, the core of the particle does not interface directly with electrolyte in a SSB, but rather would most be affected by intergranular cracking causing (partial) isolation of primary particles near the core region.

In addition to the chemical fingerprinting by means of linear combination fitting, the linear relationship between the nickel K-edge energy and SOC makes it possible to use the determined nickel oxidation state as a proxy for SOC estimations as reported in the literature.[47,50−52] We present in Figure 4d the nickel K-edge energy distribution over the *XZ* virtual slice denoted in Figure 4b. The center of Figure 4d shows lower edge energy, while the value near the particle surface becomes relative higher, suggesting higher Ni oxidation state close to the particle surface. Regardless of the methods used to evaluate the 3D-FF-TXM-XANES data, the conclusion is consistent. The core of the particle seems not able to complete the delithiation process, although the electrochemical reaction driving force is applied externally.

The core–shell separation is clearly visualized by the 3D-FF-TXM-XANES measurements that eliminate the uncertainty in the depth-averaged measurements (2D). For a more quantitative evaluation of the observed core–shell separation, we show in Figure 4e the depth profiles of the porosity and the SOC calculated from the 3D data. In this calculation, the pixels over the 3D volume are regrouped in layers with different depth from the particle surface. The average SOC and the corresponding standard deviation (the error bars) for each layer of pixels are calculated to reveal the depth dependence of the SOC. As previously discussed, while the outermost particle shell is significantly reduced, likely due to an electrolyte–electrode interface, the highest available SOC is in the particle subsurface. Past the subsurface, the SOC continuously decreases as the probing depth approaches the core. Comparing the subsurface SOC to the SOC obtained at the core, one can see a difference of about 20%. Because the SOC analysis shows a continuous decrease, cracking seems to affect redox throughout the entire particle; losses are not confined to the innermost region where the tomography shows the most severe cracking. We believe this has to do with increased particle porosity throughout its depth. Porosity is part of the structural reconstruction upon cycling and is especially prominent within the interconnected crack network shown in Figure 4a. The inverse correlation between the depth profile of the SOC and that of the porosity is worth noting, as it provides strong and direct evidence for the loss of capacity through cracking. Increased porosity leads to disruption of lithium diffusion pathways and hence makes subparticle domains less electrochemically active. While the severe crack network is very distinct near the particle's center, the porosity calculations demonstrate an impact that clearly goes beyond the particle core.

FIB/BIB-SEM Tomography. To further investigate the morphological properties of the cycled and fully charged secondary particles, high-resolution broad ion beam−secondary electron microscopy (BIB-SEM) and focused ion beam−secondary electron microscopy (FIB-SEM) tomography were used. Both methods provide deeper morphological insight with a spatial resolution significantly higher than that of the 2D- and 3D-FF-TXM data. Several cross sections of pristine pouch cells and cells that were cycled 21 times were prepared and probed using BIB-SEM at room temperature. In the same way several secondary particles were harvested from pristine and cycled cells and probed using high-resolution FIB-SEM tomography.

All analyzed cross-sectional BIB-SEM images derived from pristine cells did not show any kind of cracks, while almost all particles within cycled cross sections showed intergranular cracks (Figure 5). For statistical accuracy, many cross sections of pristine and cycled cells were analyzed (see Figures S5−S7 for pristine and Figures S8−S10 for cycled cross sections). While secondary particles in pristine cells only show densely packed primary grains, cross sections derived from cells that were cycled 21 times show cracking throughout the particles, with relatively high crack volumes in the particle centers. Furthermore, primary grains within the core seem to be more isolated due to the surrounding cracks than the grains closer to the surface of the particle. This could indicate that cracks originate in the center and propagate to the surface, as also suggested in the literature,[48,49] thereby particularly isolating primary grains in the core region of the particle (see Figures S8−S10). We believe that rapid capacity fading observed during cycling of polymer NCA cells is partly due to the vigorous intergranular cracking observed in all analyzed cross sections. This degree of cracking should lead to capacity fade, since contact between active regions is lost upon cycling and thereby spatial lithium ion transport pathways are deactivated.

If in a solid state cell we assume there is no migration of electrolyte to fill cracks, we can geometrically estimate the increased tortuosity of diffusion pathways and their effect on cell resistance using FIB-SEM tomographs. Several particles of cycled cells were harvested and analyzed by serial-sectioning and imaging using FIB-SEM. The reconstructed volume is shown in the Supporting Information (Videos S1 and S2 for pristine particles and Videos S3 and S4 for cycled particles). The secondary electron and backscattered electron images obtained from serial sectioning were analyzed using numerical modeling, as described below.

As shown in Figure 6a, in the pristine state, most of the primary particles are closely packed, although some small isolated voids are seen in the particle as highlighted by the red circles. Substantial cracks are observed in the cycled particle (Figure 6b). The cracks effectively act as physical barriers that increase the tortuosity of Li diffusion in the active material. To better understand the impact on individual primary particles caused by cracking, we adapted a numerical model that we developed recently[29] and calculated the cracking induced diffusion deterrent of the Li ions. By numerically solving the "3D maze" (as defined by the cracking pattern), starting from every single grain, the geometrically optimal Li diffusion pathway can be determined for every grain within the secondary particle. The difference in the optimal diffusion length before and after the crack formation is calculated and presented in Figure 6c,d. Here it is important to annotate that Figure 6d is essentially a differential map, derived by calculating the absolute diffusion length for every grain before and after crack formation; it highlights the cracking-caused local differences in ionic conductivity. Figure 6d is color coded to the degree of cracking-induced diffusion deterrent and is not directly proportional to the absolute diffusion length for each individual grain. More details about the model and the algorithm can be found in the paper by Xia et al.[29] The calculated results shown in Figure 6c illustrate that in pristine particles the pre-existing isolated voids have negligible impact on the Li ion diffusion. The interconnected cracks, on the other hand, cause significant rearrangement of the Li diffusion pathway, increasing values of the diffusion deterrent as shown in Figure 6d. Generally speaking, the center of the particle is more severely impacted, in good agreement with the 3D-FF-TXM-XANES data presented above.

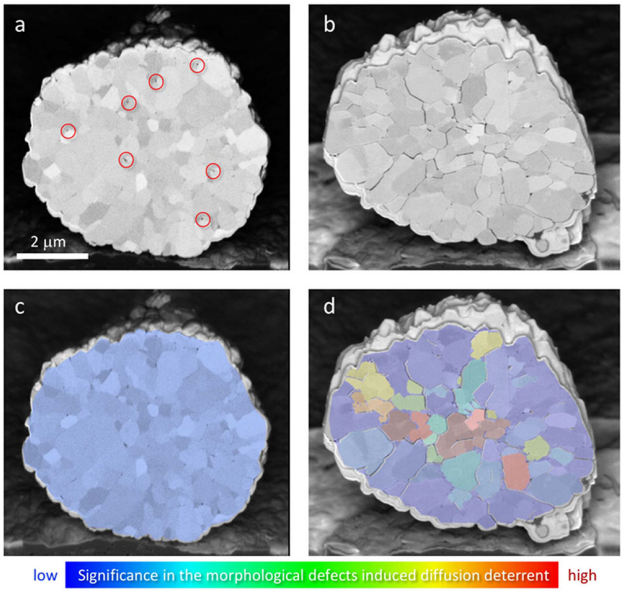

Figure 6. SEM cross-sectional image for (a) a pristine NCA secondary particle and (b) a cycled NCA secondary particle. Isolated morphological defects (see red circles in panel a) are observed in the pristine particle, while interconnected cracks are observed in the cycled particle. Panels c and d are the corresponding slices color coded to the quantification of the degree of crack induced diffusion deterrent for individual grains within the secondary particles.

To illustrate these phenomena a little more fully, Figure 7 summarizes our understanding of the impact of intergranular cracks on electron transportation and lithium ion diffusion pathways in NCA secondary particles. Figure 7a shows the geometrically optimal pathways for both charge carriers upon charging of the battery, while Figure 7b shows the change in pathways in polymer batteries upon intergranular cracking. While the geometrically shortest pathways are accessible by charge carriers in a pristine NCA particle, both electrons and lithium ions (with several orders of magnitude slower migration than electrons) must detour along a more tortuous path in a fractured particle. We hypothesize that in contrast to solid−electrolyte-based cells, intergranular cracks in conventional LiBs are filled with liquid electrolyte that facilitates Li^+ transport via two charge transfer steps (host → electrolyte → host) at intergranular cracks (Figure 7c). To support this hypothesis, we conducted an SEM-EDS experiment with cycled NCA particles that showed extensive cracks on their surface. Harvested, cycled particles were soaked in 1 M lithium hexafluorophosphate ($LiPF_6$) dissolved in a mixture of

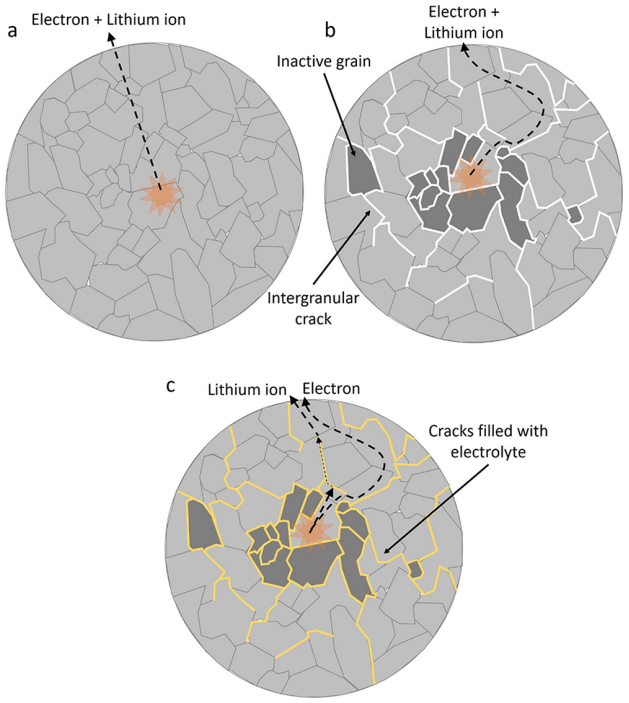

Figure 7. Schematic 2D models of a secondary NCA particles. (a) Pristine secondary NCA particle. Charge carriers transport and diffusion can happen without any barriers and the shortest geometrically ideal paths are taken. (b) Secondary NCA particle with intergranular cracks in the absence of electrolyte. Charge carriers get trapped within inactive grains and have to detour from the geometrically optimal path. (c) Secondary NCA particle with intergranular cracks in the presence of liquid electrolyte. Electrolyte can fill the cracks and only electrons have to detour the cracks, while lithium ions can still diffuse through the electrolyte-filled cracks.

ethylene carbonate (EC) and diethylene carbonate (DEC) (50:50, v/v) for 3 days and subsequently washed with salt-free EC:DEC (50:50, v/v). The particles were then subjected to an energy-dispersive X-ray spectroscopy (EDS) analysis to detect elements within intergranular cracks originating from electrolyte contact. Our EDS analysis shows a clear phosphorus signal within intergranular cracks (see Figures S11 and S12), which indicates that electrolyte diffuses into the cracks of secondary NCA particles.

In the case of liquid electrolyte, the lithium ion diffusion is faster than in a fractured particle embedded in a solid electrolyte, but the effective diffusivity is lower than in a pristine particle. However, the electrolyte does not conduct electrons, which leads to detouring of electrons due to barriers formed by the intergranular cracks. In addition, the additional charge-transfer resistance at the interfaces (host → electrolyte → host) could also influence Li ion transportation in reality. The result is a mixture of both irreversible capacity loss as well as significant growth of cell impedance, which is consistent with what we observe in the electrochemical data: when charging using a very low *C*-rate such as *C*/100, 27.81% capacity could not be regained, indicating that some primary particles have essentially become isolated. The probability of deactivation of primary grains is higher within the core region than over the outer rim of the particle, which is also reflected in our 2D and 3D-FF-TXM-XANES results.

In comparison to liquid LiBs, the amount of intergranular cracking observed for the polymer cells in this study is more severe, and the effect of cracking on capacity fade is very rapid. A detailed mechanism for the cause of rapid crack formation in NCA-PEO polymer cells is not yet wholly clear, but there are a number of possibilities. As observed in liquid LiBs, mechanical strain arising from lattice breathing or anisotropic volumetric changes upon cycling can lead to cracks in NCA particles. Oxygen release from the layered oxide, potentially exacerbated by elevated operating temperature (60−80 °C), can lead to both pressure buildup and phase transformation to a rock-salt structure, which can also cause mechanical failure. These mechanisms may be exacerbated in the polymer setting due to the pliability of the polymer electrolytes, the elevated temperature, the chemomechanical interplay with degrading PEO, high cutoff voltages, or other effects that are not yet known. A careful investigation of phase transformation within NCA particles following cycling in polymeric electrolytes, as well as a comprehensive analysis of the role of electrochemical parameters such as temperature and cutoff voltage on the rate and degree of crack formation, will be important. In addition, possible ways of avoiding intergranular cracking such as the use of single-crystalline particles,[53] atomic layer deposition (ALD) coating,[54] the use of poly(vinylidene fluoride) (PVdF) binder,[55] and the use of a lithium salt in combination with a low-viscosity polymer which could infiltrate cracks still have to be studied. A study clarifying the effects of long-term exposure of NCA to elevated operating temperatures both alone and in the presence of common polymeric electrolytes is also warranted and will be presented in a follow-up study.

CONCLUSION

Two- and three-dimensional full-field transmission X-ray microscopy was used for the first time to probe secondary NCA particles harvested from cycled NCA-PEO polymer batteries. This methodology allowed us to quantify the morphological and electrochemical changes occurring in solid-state polymer-based lithium-ion batteries. Additionally, high resolution BIB- and FIB-SEM data and a numerical model were used to estimate the deterioration in effective lithium diffusivity in fractured particles. Our study suggests that the absence of liquid electrolyte severely affects transport in fractured particles and may also hasten and accelerate fracture due to lower uniformity in current density. Intergranular cracks significantly increase diffusion path lengths of both charge carriers, electrons, and lithium ions. In liquid LiBs, electrolyte filling the cracks should maintain lithium ion transport pathways but not electron transport pathways. In solid-state LiBs, intergranular cracking compromises not only the electronic pathways but also the ionic pathways. Furthermore, intergranular cracking in NCA particles cast in a polymer matrix seems to lead to isolated and inactivated primary grains within the core of secondary particles, leading to capacity fade and reduced nickel oxidation state. While the subsurface of secondary NCA particles stays more or less intact and available for intercalation or deintercalation of lithium ions, the core of the particle loses a significant amount of its activity and contributes to the loss of capacity and rate capability.

EXPERIMENTAL SECTION

Preparation of Polymer Cells. NCA-PEO//Li cells were prepared as described in previous literature.[56−58] A polystyrene (PS)−PEO separator was used in combination with PEO binder

(electrolyte). Commercial NCA cathode material and lithium bis(trifluoromethanesulfonyl)imide (LiTFSI) were dried overnight at 120 °C. The cathode solution was prepared by dissolving 23.06 g of PEO and 10.54 g of LiTFSI in 321.46 g of analysis grade cyclohexanone. 120 g of dried NCA and 6.4 g of carbon black were then added to the mixture. The mixture was extensively mixed using a homogenizer for 45 min. The resulting slurry was immediately cast on carbon-coated aluminum current collector foil and spread evenly using a doctor blade to achieve a loading of 4.5 mg/cm^2. The electrode was dried overnight under vacuum at 70 °C. Electrodes were punched into 10 cm^2 pieces and pressed on a 40 μm PS−PEO polymer electrolyte film. A 60 μm lithium metal anode was pressed on the other side of the PS−PEO polymer electrolyte. The cell stack was then assembled in a pouch cell with a nickel terminal on the negative electrode and an aluminum tab on the positive electrode. The pouch cell was then sealed in an aluminum-laminated pouch material using a vacuum sealer in a dry room for an air-free atmosphere.

Electrochemical Cycling. The pouch cells were cycled with an Arbin BT2043 tester at 80 °C. Galvanostatic cycling was performed at a rate of *C*/6 referring to a practical capacity of NCA of 180 mAh/g between 3 and 4.2 V; this *C*-rate corresponds to a current density of 100 μA/cm^2. A stack pressure of 5 psi was applied during electrochemical cycling. No difference in electrochemical performance was found at higher stack pressures.

Materials Characterization. Hard XAS data on Ni K-edge were collected in transmission mode using a Si (220) monochromator at SSRL beamline 4-1. NCA-PEO//lithium polymer cells (pristine, single-charged and cycled) were used as-prepared during the measurement. Higher harmonics in the X-ray beam were rejected by detuning the Si (220) monochromator by 40% at the nickel edge. Energy calibration was accomplished by using the first inflection points in the spectra of nickel metal foil reference at 8332.8 eV. XANES data were analyzed by Sam's Interface for XAS Package (SIXPACK), with the photoelectron energy origin (E_0) determined by the first inflection point of the absorption edge jump.

NCA particles were harvested from pristine, single-charged, and cycled cells. The polymer pouch cells were cut open using a ceramic knife in an argon-filled glovebox (O_2 < 0.1 ppm and H_2O < 0.1 ppm). The metallic lithium anode was carefully separated from the NCA cathode. Acetonitrile was used to dissolve and separate NCA particles form the NCA-PEO electrode by centrifugation. After washing the harvested NCA cathode material several times with acetonitrile, material was dried under vacuum for 48 h and sealed and stored in an argon-filled glovebox.

FF-TXM imaging was performed at the 54 pole wiggler beamline 6-2c at the SSRL. The detailed beamline configuration can be found in a previous report.[59] Harvested NCA particles were carefully dispersed in cylindrical quartz capillaries (100 μm in diameter and 10 μm in wall thickness) and carefully mounted to the beamline sample holder. Slow and steady helium gas flow was applied to the capillaries to minimize the radiation-induced heat load on the sample during the scans and also to prevent air exposure. The X-ray energy was tuned to nickel K-edge and then focused onto the sample by an elliptically shaped capillary condenser providing illumination for a FOV of approximately 30 × 30 μm^2. The 2D transmission images (0.5 s exposure time, 10 repetitions, binning 2, 1024 × 1024 pixels) were collected from 8100 to 8800 eV in 134 steps for each sample. To remove distortions caused by the flux and beam instabilities, concurrent acquisition of reference images at each energy was also performed through an open area of the sample (outside the capillary) with the same imaging configuration. The repetitions in exposures were performed to enhance the dynamic range of the existing charge-coupled device and, subsequently, improve the signal-to-noise ratio in the data. 3D-FF-TXM-XANES tomography was performed by rotating the quartz capillaries from −90° to 90° with an angular step size of 1° and 58 different energy steps across the nickel K-edge. The tomographic reconstruction and data analysis were performed using TXM-Wizard, an in-house-developed software package. The effective 3D voxel size is 32.5 × 32.5 × 32.5 nm^3.

FIB-SEM of pristine and cycled harvested particles was performed using a Helios G4 dual-beam FIB. Sectioning of particles was performed using gallium ions at 30 kV, which were imaged using electrons at 5 kV. The currents used for ion and electron beams were 26 pA and 0.4 nA, respectively. Secondary electron as well as backscattered electron detectors were used for imaging. Serial-sectioning and SEM imaging were done every 10 nm, and the images were aligned and reconstructed to create a 3D volume of entire secondary particles.

SEM imaging was utilized for pristine and cycled cross sections of cells that were previously cut with a ceramic knife using a Hitachi High-Tech Ltd. S-4800 microscope (accelerating voltage 1.5 kV) equipped with a Bruker AXS Ltd. QUANTAX FlatQUAD System Xflash 5060FQ (accelerating voltage 5 kV). Prior to loading the SEM specimen under an argon gas atmosphere to the sample holder using an atmospherically isolated transfer vessel to prevent exposure to air, cross-sectional BIB milling was conducted using a JEOL Ltd. IB-19520CCP.

AUTHOR INFORMATION

Corresponding Authors

*(S.K.) E-mail saravanan.kuppan@us.bosch.com.
*(M.D.) E-mail mmdoeff@lbl.gov.
*(Y.L.) E-mail liuyijin@slac.stanford.edu.

ORCID

Saravanan Kuppan: 0000-0003-4976-4514
Michael Metzger: 0000-0002-5512-8541
Marca M. Doeff: 0000-0002-2148-8047
Yijin Liu: 0000-0002-8417-2488

Notes

The authors declare no competing financial interest.

ACKNOWLEDGMENTS

The synchrotron experiments of this research were performed at the SSRL, a Directorate of SLAC National Accelerator Laboratory and an Office of Science User Facility operated for the U.S. Department of Energy Office of Science by Stanford University. Use of the Stanford Synchrotron Radiation Lightsource, SLAC National Accelerator Laboratory, is supported by the U.S. Department of Energy, Office of Science, Office of Basic Energy Sciences under Contract DE-AC02-76SF00515. We thank Drs. Erik Nelson, Matthew Latimer, and Ryan Davis for assisting with the synchrotron experiments. Work at the Molecular Foundry was supported by the Office of Science, Office of Basic Energy Sciences, of the U.S. Department of Energy under Contract DE-AC02-05CH11231. The engineering support from D. Van Campen,

D. Day, and V. Borzenets for the TXM experiment at beamline 6-2C of SSRL is gratefully acknowledged.

REFERENCES

(1) Lin, C.; Tang, A.; Mu, H.; Wang, W.; Wang, C. Aging Mechanisms of Electrode Materials in Lithium-Ion Batteries for Electric Vehicles. *J. Chem.* **2015**, *2015*, 104673.

(2) Perner, A.; Vetter, J. Lithium-Ion Batteries for Hybrid Electric Vehicles and Battery Electric Vehicles. In *Advances in Battery Technologies for Electric Vehicles*; Scrosati, B., Garche, J., Tillmetz, W., Eds.; Woodhead Publishing Series in Energy; Elsevier: 2015; pp 173−190.

(3) Dunn, B.; Kamath, H.; Tarascon, J.-M. Electrical Energy Storage for the Grid: A Battery of Choices. *Science (Washington, DC, U. S.)* **2011**, *334* (6058), 928−935.

(4) Sharafi, A.; Kazyak, E.; Davis, A. L.; Yu, S.; Thompson, T.; Siegel, D. J.; Dasgupta, N. P.; Sakamoto, J. Surface Chemistry Mechanism of Ultra-Low Interfacial Resistance in the Solid-State Electrolyte $Li_7La_3Zr_2O_{12}$. *Chem. Mater.* **2017**, *29* (18), 7961−7968.

(5) Kazyak, E.; Chen, K.-H.; Wood, K. N.; Davis, A. L.; Thompson, T.; Bielinski, A. R.; Sanchez, A. J.; Wang, X.; Wang, C.; Sakamoto, J.; et al. Atomic Layer Deposition of the Solid Electrolyte Garnet $Li_7La_3Zr_2O_{12}$. *Chem. Mater.* **2017**, *29* (8), 3785−3792.

(6) Inoue, T.; Mukai, K. Are All-Solid-State Lithium-Ion Batteries Really Safe?−Verification by Differential Scanning Calorimetry with an All-Inclusive Microcell. *ACS Appl. Mater. Interfaces* **2017**, *9* (2), 1507−1515.

(7) Thangadurai, V.; Weppner, W. Recent Progress in Solid Oxide and Lithium Ion Conducting Electrolytes Research. *Ionics* **2006**, *12* (1), 81−92.

(8) Tarascon, J. M.; Armand, M. Issues and Challenges Facing Rechargeable Lithium Batteries. *Nature* **2001**, *414* (6861), 359−367.

(9) Manthiram, A.; Song, B.; Li, W. A Perspective on Nickel-Rich Layered Oxide Cathodes for Lithium-Ion Batteries. *Energy Storage Mater.* **2017**, *6*, 125−139.

(10) Mukhopadhyay, A.; Sheldon, B. W. Deformation and Stress in Electrode Materials for Li-Ion Batteries. *Prog. Mater. Sci.* **2014**, *63*, 58−116.

(11) Makimura, Y.; Zheng, S.; Ikuhara, Y.; Ukyo, Y. Microstructural Observation of $LiNi_{0.8}Co_{0.15}Al_{0.05}O_2$ after Charge and Discharge by Scanning Transmission Electron Microscopy. *J. Electrochem. Soc.* **2012**, *159* (7), A1070−A1073.

(12) Lim, J.-M.; Hwang, T.; Kim, D.; Park, M.-S.; Cho, K.; Cho, M. Intrinsic Origins of Crack Generation in Ni-Rich $LiNi_{0.8}Co_{0.1}Mn_{0.1}O_2$ Layered Oxide Cathode Material. *Sci. Rep.* **2017**, *7* (1), 39669.

(13) Sun, H.-H.; Manthiram, A. Impact of Microcrack Generation and Surface Degradation on a Nickel-Rich Layered $Li[Ni_{0.9}Co_{0.05}Mn_{0.05}]O_2$ Cathode for Lithium-Ion Batteries. *Chem. Mater.* **2017**, *29* (19), 8486−8493.

(14) Kojima, Y.; Muto, S.; Tatsumi, K.; Kondo, H.; Oka, H.; Horibuchi, K.; Ukyo, Y. Degradation Analysis of a Ni-Based Layered Positive-Electrode Active Material Cycled at Elevated Temperatures Studied by Scanning Transmission Electron Microscopy and Electron Energy-Loss Spectroscopy. *J. Power Sources* **2011**, *196* (18), 7721−7727.

(15) Watanabe, S.; Kinoshita, M.; Hosokawa, T.; Morigaki, K.; Nakura, K. Capacity Fading of $LiAl_yNi_{1-x-y}Co_xO_2$ cathode for Lithium-Ion Batteries during Accelerated Calendar and Cycle Life Tests (Effect of Depth of Discharge in Charge-Discharge Cycling on the Suppression of the Micro-Crack Generation of $LiAl_yNi_{1-x-y}Co_xO_2$ particle). *J. Power Sources* **2014**, *260*, 50−56.

(16) Faenza, N. V.; Lebens-Higgins, Z. W.; Mukherjee, P.; Sallis, S.; Pereira, N.; Badway, F.; Halajko, A.; Ceder, G.; Cosandey, F.; Piper, L. F. J.; et al. Electrolyte-Induced Surface Transformation and Transition-Metal Dissolution of Fully Delithiated $LiNi_{0.8}Co_{0.15}Al_{0.05}O_2$. *Langmuir* **2017**, *33* (37), 9333−9353.

(17) Tian, C.; Xu, Y.; Nordlund, D.; Lin, F.; Liu, J.; Sun, Z.; Liu, Y.; Doeff, M. Charge Heterogeneity and Surface Chemistry in Polycrystalline Cathode Materials. *Joule* **2018**, *2* (3), 464−477.

(18) Park, S. Y.; Baek, W. J.; Lee, S. Y.; Seo, J. A.; Kang, Y.-S.; Koh, M.; Kim, S. H. Probing Electrical Degradation of Cathode Materials for Lithium-Ion Batteries with Nanoscale Resolution. *Nano Energy* **2018**, *49*, 1−6.

(19) Huang, R.; Ikuhara, Y. STEM Characterization for Lithium-Ion Battery Cathode Materials. *Curr. Opin. Solid State Mater. Sci.* **2012**, *16* (1), 31−38.

(20) Mu, L.; Lin, R.; Xu, R.; Han, L.; Xia, S.; Sokaras, D.; Steiner, J. D.; Weng, T. C.; Nordlund, D.; Doeff, M. M.; et al. Oxygen Release Induced Chemomechanical Breakdown of Layered Cathode Materials. *Nano Lett.* **2018**, *18* (5), 3241−3249.

(21) Christensen, J. Modeling Diffusion-Induced Stress in Li-Ion Cells with Porous Electrodes. *J. Electrochem. Soc.* **2010**, *157* (3), A366−A380.

(22) Christensen, J.; Newman, J. Stress Generation and Fracture in Lithium Insertion Materials. *J. Solid State Electrochem.* **2006**, *10* (5), 293−319.

(23) Cheng, Y. T.; Verbrugge, M. W. Evolution of Stress within a Spherical Insertion Electrode Particle under Potentiostatic and Galvanostatic Operation. *J. Power Sources* **2009**, *190* (2), 453−460.

(24) Woodford, W. H.; Chiang, Y.-M.; Carter, W. C. "Electrochemical Shock" of Intercalation Electrodes: A Fracture Mechanics Analysis. *J. Electrochem. Soc.* **2010**, *157* (10), A1052−A1059.

(25) Woo, S. G.; Kim, J. H.; Kim, H. R.; Cho, W.; Yu, J. S. Failure Mechanism Analysis of $LiNi_{0.88}Co_{0.09}Mn_{0.03}O_2$ cathodes in Li-Ion Full Cells. *J. Electroanal. Chem.* **2017**, *799* (April), 315−320.

(26) Yan, P.; Zheng, J.; Gu, M.; Xiao, J.; Zhang, J.-G.; Wang, C.-M. Intragranular Cracking as a Critical Barrier for High-Voltage Usage of Layer-Structured Cathode for Lithium-Ion Batteries. *Nat. Commun.* **2017**, *8*, 14101.

(27) Zheng, J.; Yan, P.; Zhang, J.; Engelhard, M. H.; Zhu, Z.; Polzin, B. J.; Trask, S.; Xiao, J.; Wang, C.; Zhang, J. Suppressed Oxygen Extraction and Degradation of $LiNi_xMn_yCo_zO_2$ cathodes at High Charge Cut-off Voltages. *Nano Res.* **2017**, *10* (12), 4221−4231.

(28) Lang, M.; Darma, M. S. D.; Kleiner, K.; Riekehr, L.; Mereacre, L.; Ávila Pérez, M.; Liebau, V.; Ehrenberg, H. Post Mortem Analysis of Fatigue Mechanisms in $LiNi_{0.8}Co_{0.15}Al_{0.05}O_2$ − $LiNi_{0.5}Co_{0.2}Mn_{0.3}O_2$ − $LiMn_2O_4$/Graphite Lithium Ion Batteries. *J. Power Sources* **2016**, *326*, 397−409.

(29) Xia, S.; Mu, L.; Xu, Z.; Wang, J.; Wei, C.; Liu, L.; Pianetta, P.; Zhao, K.; Yu, X.; Lin, F.; Liu, Y. Chemomechanical Breakdown of Layered Cathode Materials Undergoing Fast Charging in Lithium Batteries. *Nano Energy* **2018**, *53*, 753−762.

(30) Yoon, C. S.; Park, K.-J.; Kim, U.-H.; Kang, K. H.; Ryu, H.-H.; Sun, Y.-K. High-Energy Ni-Rich $Li[Ni_xCo_yMn_{1-x-y}]O_2$ Cathodes via Compositional Partitioning for Next-Generation Electric Vehicles. *Chem. Mater.* **2017**, *29* (24), 10436−10445.

(31) Kim, H.-R.; Woo, S.-G.; Kim, J.-H.; Cho, W.; Kim, Y.-J. Capacity Fading Behavior of Ni-Rich Layered Cathode Materials in Li-Ion Full Cells. *J. Electroanal. Chem.* **2016**, *782*, 168−173.

(32) Wu, L.; Nam, K.-W.; Wang, X.; Zhou, Y.; Zheng, J.-C.; Yang, X.-Q.; Zhu, Y. Structural Origin of Overcharge-Induced Thermal Instability of Ni-Containing Layered-Cathodes for High-Energy-Density Lithium Batteries. *Chem. Mater.* **2011**, *23* (17), 3953−3960.

(33) Bak, S. M.; Nam, K. W.; Chang, W.; Yu, X.; Hu, E.; Hwang, S.; Stach, E. A.; Kim, K. B.; Chung, K. Y.; Yang, X. Q. Correlating Structural Changes and Gas Evolution during the Thermal Decomposition of Charged $Li_xNi_{0.8}Co_{0.15}Al_{0.05}O_2$ Cathode Materials. *Chem. Mater.* **2013**, *25* (3), 337−351.

(34) Boyd, J. W.; Schmalzl, P. W.; Miller, L. L. Mechanism of Anodic Cleavage of Benzyl Ethers. *J. Am. Chem. Soc.* **1980**, *102* (11), 3856−3862.

(35) Ma, T.; Xu, G.-L.; Li, Y.; Wang, L.; He, X.; Zheng, J.; Liu, J.; Engelhard, M. H.; Zapol, P.; Curtiss, L. A.; et al. Revisiting the Corrosion of the Aluminum Current Collector in Lithium-Ion Batteries. *J. Phys. Chem. Lett.* **2017**, *8* (5), 1072−1077.

(36) Balasubramanian, M.; Sun, X.; Yang, X. Q.; Mcbreen, J. In Situ X-Ray Absorption Studies of a High-Rate $LiNi_{0.85}Co_{0.15}O_2$ Cathode Material. *J. Electrochem. Soc.* **2000**, *147* (8), 2903−2909.

(37) Saravanan, K.; Jarry, A.; Kostecki, R.; Chen, G. A Study of Room-Temperature $Li_xMn_{1.5}Ni_{0.5}O_4$ Solid Solutions. *Sci. Rep.* **2015**, *5* (1), 8027.
(38) Kuppan, S.; Duncan, H.; Chen, G. Controlling Side Reactions and Self-Discharge in High-Voltage Spinel Cathodes: The Critical Role of Surface Crystallographic Facets. *Phys. Chem. Chem. Phys.* **2015**, *17* (39), 26471−26481.
(39) Lin, F.; Nordlund, D.; Markus, I. M.; Weng, T. C.; Xin, H. L.; Doeff, M. M. Profiling the Nanoscale Gradient in Stoichiometric Layered Cathode Particles for Lithium-Ion Batteries. *Energy Environ. Sci.* **2014**, *7* (9), 3077−3085.
(40) Hwang, S.; Chang, W.; Kim, S. M.; Su, D.; Kim, D. H.; Lee, J. Y.; Chung, K. Y.; Stach, E. A. Investigation of Changes in the Surface Structure of $Li_xNi_{0.8}Co_{0.15}Al_{0.05}O_2$ Cathode Materials Induced by the Initial Charge. *Chem. Mater.* **2014**, *26* (2), 1084−1092.
(41) Lin, F.; Markus, I. M.; Nordlund, D.; Weng, T.-C.; Asta, M. D.; Xin, H. L.; Doeff, M. M. Surface Reconstruction and Chemical Evolution of Stoichiometric Layered Cathode Materials for Lithium-Ion Batteries. *Nat. Commun.* **2014**, *5* (1), 3529.
(42) Sumathipala, H. H.; Hassoun, J.; Panero, S.; Scrosati, B. High Performance PEO-Based Polymer Electrolytes and Their Application in Rechargeable Lithium Polymer Batteries. *Ionics* **2007**, *13* (5), 281−286.
(43) Wei, C.; Xia, S.; Huang, H.; Mao, Y.; Pianetta, P.; Liu, Y. Mesoscale Battery Science: The Behavior of Electrode Particles Caught on a Multispectral X-Ray Camera. *Acc. Chem. Res.* **2018**, *51* (10), 2484−2492.
(44) Liu, Y.; Meirer, F.; Williams, P. A.; Wang, J.; Andrews, J. C.; Pianetta, P. TXM-Wizard: A Program for Advanced Data Collection and Evaluation in Full-Field Transmission X-Ray Microscopy. *J. Synchrotron Radiat.* **2012**, *19* (2), 281−287.
(45) Meirer, F.; Cabana, J.; Liu, Y.; Mehta, A.; Andrews, J. C.; Pianetta, P. Three-Dimensional Imaging of Chemical Phase Transformations at the Nanoscale with Full-Field Transmission X-Ray Microscopy. *J. Synchrotron Radiat.* **2011**, *18* (5), 773−781.
(46) Kao, T. L.; Shi, C. Y.; Wang, J.; Mao, W. L.; Liu, Y.; Yang, W. Nanoscale Elemental Sensitivity Study of $Nd_2Fe_{14}B$ Using Absorption Correlation Tomography. *Microsc. Res. Technol.* **2013**, *76* (11), 1112−1117.
(47) Kuppan, S.; Xu, Y.; Liu, Y.; Chen, G. Phase Transformation Mechanism in Lithium Manganese Nickel Oxide Revealed by Single-Crystal Hard X-Ray Microscopy. *Nat. Commun.* **2017**, *8*, 14309.
(48) Tsai, P.-C.; Wen, B.; Wolfman, M.; Choe, M.-J.; Pan, M. S.; Su, L.; Thornton, K.; Cabana, J.; Chiang, Y.-M. Single-Particle Measurements of Electrochemical Kinetics in NMC and NCA Cathodes for Li-Ion Batteries. *Energy Environ. Sci.* **2018**, *11* (4), 860−871.
(49) Zhang, H.; Omenya, F.; Whittingham, M. S.; Wang, C.; Zhou, G. Formation of an Anti-Core-Shell Structure in Layered Oxide Cathodes for Li-Ion Batteries. *ACS Energy Lett.* **2017**, *2* (11), 2598−2606.
(50) Yoon, W.-S.; Balasubramanian, M.; Chung, K. Y.; Yang, X.-Q.; McBreen, J.; Grey, C. P.; Fischer, D. A. Investigation of the Charge Compensation Mechanism on the Electrochemically Li-Ion Deintercalated $Li_{1-X}Co_{1/3}Ni_{1/3}Mn_{1/3}O_2$ Electrode System by Combination of Soft and Hard X-Ray Absorption Spectroscopy. *J. Am. Chem. Soc.* **2005**, *127* (49), 17479−17487.
(51) Rumble, C.; Conry, T. E.; Doeff, M.; Cairns, E. J.; Penner-Hahn, J. E.; Deb, A. Structural and Electrochemical Investigation of $Li(Ni_{0.4}Co_{0.15}Al_{0.05}Mn_{0.4})O_2$ Cathode Material. *J. Electrochem. Soc.* **2010**, *157* (12), A1317.
(52) Xu, J.; Lin, F.; Doeff, M. M.; Tong, W. A Review of Ni-Based Layered Oxides for Rechargeable Li-Ion Batteries. *J. Mater. Chem. A* **2017**, *5* (3), 874−901.
(53) Liu, G.; Li, M.; Wu, N.; Cui, L.; Huang, X.; Liu, X.; Zhao, Y.; Chen, H.; Yuan, W.; Bai, Y. Single-Crystalline Particles: An Effective Way to Ameliorate the Intragranular Cracking, Thermal Stability, and Capacity Fading of the $LiNi_{0.6}Co_{0.2}Mn_{0.2}O_2$ Electrodes. *J. Electrochem. Soc.* **2018**, *165* (13), A3040−A3047.
(54) Mohanty, D.; Dahlberg, K.; King, D. M.; David, L. A.; Sefat, A. S.; Wood, D. L.; Daniel, C.; Dhar, S.; Mahajan, V.; Lee, M.; Albano, F. Modification of Ni-Rich FCG NMC and NCA Cathodes by Atomic Layer Deposition: Preventing Surface Phase Transitions for High-Voltage Lithium-Ion Batteries. *Sci. Rep.* **2016**, *6* (1), 26532.
(55) Tsai, P. C.; Wen, B.; Wolfman, M.; Choe, M. J.; Pan, M. S.; Su, L.; Thornton, K.; Cabana, J.; Chiang, Y. M. Single-Particle Measurements of Electrochemical Kinetics in NMC and NCA Cathodes for Li-Ion Batteries. *Energy Environ. Sci.* **2018**, *11* (4), 860−871.
(56) Panday, A.; Mullin, S.; Gomez, E. D.; Wanakule, N.; Chen, V. L.; Hexemer, A.; Pople, J.; Balsara, N. P. Effect of Molecular Weight and Salt Concentration on Conductivity of Block Copolymer Electrolytes. *Macromolecules* **2009**, *42* (13), 4632−4637.
(57) Javier, A. E.; Patel, S. N.; Hallinan, D. T.; Srinivasan, V.; Balsara, N. P. Simultaneous Electronic and Ionic Conduction in a Block Copolymer: Application in Lithium Battery Electrodes. *Angew. Chem., Int. Ed.* **2011**, *50* (42), 9848−9851.
(58) Wu, S.-L.; Javier, A. E.; Devaux, D.; Balsara, N. P.; Srinivasan, V. Discharge Characteristics of Lithium Battery Electrodes with a Semiconducting Polymer Studied by Continuum Modeling and Experiment. *J. Electrochem. Soc.* **2014**, *161* (12), A1836−A1843.
(59) Liu, Y.; Andrews, J. C.; Wang, J.; Meirer, F.; Zhu, P.; Wu, Z.; Pianetta, P. Phase Retrieval Using Polychromatic Illumination for Transmission X-Ray Microscopy. *Opt. Express* **2011**, *19* (2), 540.